Motion artefact detection in structured illumination microscopy for live cell imaging

RONNY FÖRSTER,[1,2,*] KAI WICKER,[3] WALTER MÜLLER,[1,2] AURÉLIE JOST,[1,2] AND RAINER HEINTZMANN[1,2]

[1]*Leibniz Institute of Photonic Technology, Albert-Einstein-Strasse 9, 07745 Jena, Germany*
[2]*Institute for Physical Chemistry, Abbe Center of Photonics, Friedrich-Schiller University, Helmholtzweg 4, 07743 Jena, Germany*
[3]*Carl Zeiss AG, Corporate Research and Technology, Carl-Zeiss-Promenade 10, 07745 Jena, Germany*
[*]ronny.foerster.jena@gmail.com

Abstract: The reconstruction process of structured illumination microscopy (SIM) creates substantial artefacts if the specimen has moved during the acquisition. This reduces the applicability of SIM for live cell imaging, because these artefacts cannot always be recognized as such in the final image. A movement is not necessarily visible in the raw data, due to the varying excitation patterns and the photon noise. We present a method to detect motion by extracting and comparing two independent 3D wide-field images out of the standard SIM raw data without needing additional images. Their difference reveals moving objects overlaid with noise, which are distinguished by a probability theory-based analysis. Our algorithm tags motion-artefacts in the final high-resolution image for the first time, preventing the end-user from misinterpreting the data. We show and explain different types of artefacts and demonstrate our algorithm on a living cell.

References and links

1. R. Heintzmann and C. Cremer, "Laterally modulated excitation microscopy: improvement of resolution by using a diffraction grating," Proc. SPIE **3568**, 185–196 (1999).
2. M. G. L. Gustafsson, "Surpassing the lateral resolution limit by a factor of two using structured illumination microscopy," J. Microsc. **198**(2), 82–87 (2000).
3. M. G. L. Gustafsson, L. Shao, P. M. Carlton, C. J. R. Wang, I. N. Golubovskaya, W. Z. Cande, D. A. Agard, and J. W. Sedat, "Three-dimensional resolution doubling in wide-field fluorescence microscopy by structured illumination," Biophys. J. **94**(12), 4957–4970 (2008).
4. Nikon Corporation, "Super resolution microscope N-SIM E," https://www.nikoninstruments.com/content/download/18277/440857/file/N-SIM_E_2CE-SCMH.pdf.
5. G. E. Healthcare, "DeltaVision™ OMX SR super-resolution microscope," https://www.gelifesciences.com/gehcls_images/GELS/Related Content/Files/1435762098806/litdoc29146719_20150701164816.pdf.
6. L. M. Hirvonen, K. Wicker, O. Mandula, and R. Heintzmann, "Structured illumination microscopy of a living cell," Eur. Biophys. J. **38**(6), 807–812 (2009).
7. P. Kner, B. B. Chhun, E. R. Griffis, L. Winoto, and M. G. L. Gustafsson, "Super-resolution video microscopy of live cells by structured illumination," Nat. Methods **6**(5), 339–342 (2009).
8. R. Förster, H.-W. Lu-Walther, A. Jost, M. Kielhorn, K. Wicker, and R. Heintzmann, "Simple structured illumination microscope setup with high acquisition speed by using a spatial light modulator," Opt. Express **22**(17), 20663–20677 (2014).
9. H.-W. Lu-Walther, M. Kielhorn, R. Förster, A. Jost, K. Wicker, and R. Heintzmann, "fastSIM: a practical implementation of fast structured illumination microscopy," Methods Appl. Fluoresc. **3**(1), 014001 (2015).
10. L. Song, H.-W. Lu-Walther, R. Förster, A. Jost, M. Kielhorn, J. Zhou, and R. Heintzmann, "Fast structured illumination microscopy using rolling shutter cameras," Meas. Sci. Technol. **27**(5), 055401 (2016).
11. T. Xia, N. Li, and X. Fang, "Single-molecule fluorescence imaging in living cells," Annu. Rev. Phys. Chem. **64**(1), 459–480 (2013).
12. K. Wicker and R. Heintzmann, "Single-shot optical sectioning using polarization-coded structured illumination," J. Opt. **12**(8), 084010 (2010).

13. J. R. Lakowicz, *Principles of Fluorescence Spectroscopy* (Springer Science, 2006).
14. I. Rumak, R. Mazur, K. Gieczewska, J. Kozioł-Lipińska, B. Kierdaszuk, W. P. Michalski, B. J. Shiell, J. H. Venema, W. J. Vredenberg, A. Mostowska, and M. Garstka, "Correlation between spatial (3D) structure of pea and bean thylakoid membranes and arrangement of chlorophyll-protein complexes," BMC Plant Biol. **12**(1), 72 (2012).

1. Introduction

Structured illumination microscopy (SIM) is a well-established high-resolution microscopy technique in biomedical research. A combination of several wide-field raw-images, each acquired with a different sinusoidal excitation pattern, yields a high-resolution image. Figures 1 and 2 illustrate and recapitulate the acquisition procedure in real and Fourier space respectively.
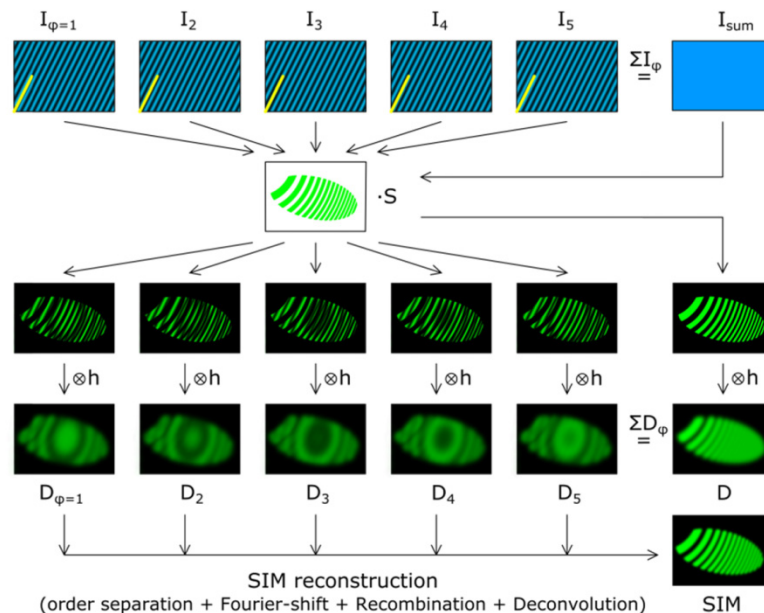

Fig. 1. Summary three-beam SIM: The specimen S is illuminated with several fine sinusoidal excitation patterns I_φ (top row). High sample frequencies are down-modulated and form coarse interference fringes (middle row), which are well transferred by the objective. The images D_φ (bottom row) are formed by a convolution with the PSF h. The reconstruction algorithm converts the down-modulated low-frequency fringes back to their original frequency, which is beyond the Abbe-limit. Thus the SIM image has a higher resolution than the wide-field image D. The necessary conversion needs typically $\phi = 5$ different raw images, to separate 5 different intensity orders overlapping in Fourier space. Thus, 5 images D_φ of the sample are acquired with 5 different excitation patterns I_φ, which differ only in a lateral shift called phase φ. The small shift can be seen best at the fixed yellow reference line (for visualization purpose only). All five excitation patterns add up to a homogeneous pattern I_{sum}, so that no residual pattern is bleached into the specimen. In order to achieve an isotropic resolution enhancement, this procedure has to be repeated three times, while the grating is rotated by 60° after every five images. Hence there are 15 raw images per focus slice. Acquiring them at every focus position creates a 3D raw data stack, which contains typically around 300 million pixels $([x,y,\phi,z] = [1000,1000,15,20])$ for each colour and timeframe.
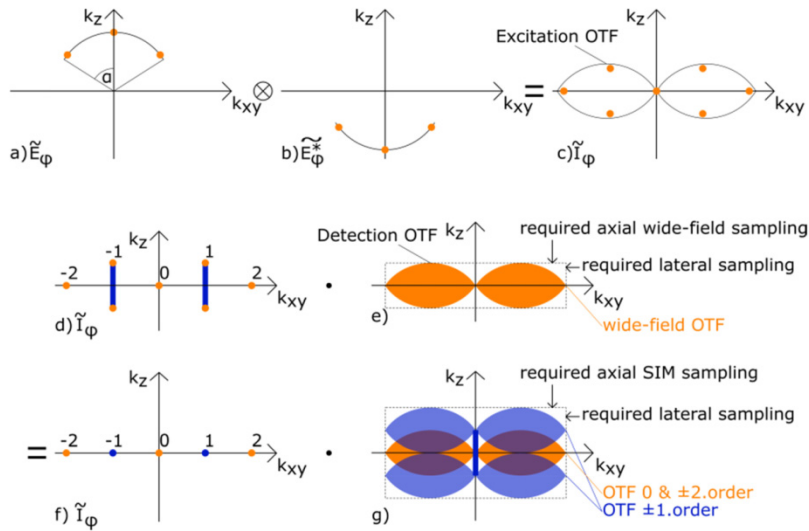
Fig. 2. Overview of SIM orders in Fourier space: a) 3 excitation beams $\tilde{E}_\varphi\left(\vec{k}\right)$ with phase φ are focused in the back focal plane (BFP) of the objective (orange dots). They form three interfering plane waves $E_\varphi\left(\vec{r}\right)$ in the specimen. b) Complex conjugated beams $\tilde{E}_\varphi^*\left(\vec{k}\right)$; c) The excitation pattern in the specimen $I_\varphi\left(\vec{r}\right)$ is $\tilde{E}_\varphi\left(\vec{k}\right)\cdot\tilde{E}_\varphi^*\left(\vec{k}\right)$. As a result, the excitation pattern represented in Fourier space is the autocorrelation of the incoming beams: $\tilde{I}_\varphi\left(\vec{k}\right)=\tilde{E}_\varphi\left(\vec{k}\right)\otimes\tilde{E}_\varphi^*\left(\vec{k}\right)$. This leads to 7 SIM illumination intensity peaks (orange dots). d) The sample information is attached to each of them, causing the down modulation of high frequency information, before the multiplicative low-pass of the OTF (shown in e) damps or removes it. This artificial frequency shift needs to be undone so that the precious transferred high frequency components are placed at their true original position. However, all SIM orders are always present at the same time in each single raw image, so that they need to be separated from each other. This can be done by exploiting the individual phase of each illumination intensity peak, which can be controlled by a shift of the excitation pattern in the sample plane. Thus, SIM needs as many images with different phases as orders. Unfortunately, the first order pairs modulate identical and cannot be separated. However, they only differ by their axial shift in Fourier space (blue line in panel d). Since the 3D illumination structure is refocussing with the sample refocus, each such pair automatically demodulates, leading to an axially enlarged effective detection OTF (blue OTF in panel g). Thus, only 5 independent SIM orders remain (panel f) with different effective detection OTFs. However, the axial sampling has to be doubled to avoid aliasing in the axial direction because of the extended frequency support of the two detection OTFs [1–3].

The optical transfer function (OTF) is extended by a factor of two in the lateral plane and the missing cone is filled [1–3]. Commercial three-beam systems typically reach a lateral and axial resolution down to 115 nm and 269 nm respectively [4]. However, SIM requires a stable specimen while acquiring the raw-images. Any movement in the range of a fraction of the point spread functions (PSF) width will lead to artefacts, which often cannot be detected as such. Unfortunately, even the fastest currently commercially available system needs 2.4 s to image a 3µm thick slice [5]. Thus, living cells in biomedical research are prone to motion-artefacts and have to be fixed in order to ensure an artefact-free image of high resolution. This fact limits the practical use of SIM. To overcome this problem, the acquisition time has been reduced in the last decade. Slow diffraction gratings have been replaced by fast spatial light modulators (SLM), in order to reduce the lost time to switch between two different illumination patterns [6–9]. Modern cameras still improve in readout speed and quantum efficiency. In addition, permanent image exposure - even during the camera read out - further

improves the frame rate [10]. The fluorescent signal has been increased by making high power lasers affordable and the persistent research on fluorophores with the necessary photostability and high quantum yield [11]. A completely different approach is single-shot SIM [12]. However, this method has not yet been demonstrated in practise and useful mostly to obtain optical sectioning rather than resolution enhancement.

Regardless of future improvements in the acquisition speed of SIM, there are still fluorescent objects that move too fast and produce unpredictable artefacts. In order to establish SIM in life science, the end users have to know whether the high-resolution image of their specimen shows reality or artefacts. Our algorithm aims to answer this question and prevents the end user from misinterpreting the images.

2. Theory

Motion is defined as a change of position with time. Thus, motion can be revealed by comparing two consecutive images of the same scene. Any change can be detected and especially located in the pixelwise difference of both images, as a non-zero value. This *frame difference method* (FDM) is a standard technique but has its requirements on both images:

A) The illumination has to stay the same, because a change of object brightness is visible in the difference image even for fixed objects.

B) The imaging optics has to keep its focus. Subtracting a sharp of a blurry image of the same object will lead to a non-zero FDM signal.

C) The number of photons has to be high enough, so that a change in the object is not lost in the photon/shot noise and the readout noise of the camera sensor. Thus, the brighter an object, the better its motion can be identified.

None of these criteria are automatically fulfilled in SIM. In order to use the FDM, the data needs to be pre-processed. The following subsections show how the three required conditions can be fulfilled step-by-step using standard SIM raw data, which is illustrated in Fig. 3.

2.1 Step A - create pseudo wide-field image

The periodic but inhomogeneous illumination pattern typically changes after each acquired raw image. As a result, a single fluorophore can for example disappear from one image to another for two reasons: either by a real physical movement to a different position, or by simply residing on a dark excitation fringe. It is close to impossible to distinguish between both possibilities from just looking at two consecutive frames. Thus, one solution is to acquire a standard wide-field image before and after all SIM images have been acquired in one plane. However, acquiring two additional images to the already existing 15 per slice will extend the acquisition time by 13% and leads to more phototoxicity. A solution without additional images or changing the standard acquisition protocol is desirable. Fortunately, to avoid inhomogeneous bleaching and to get the best separation of the orders, the phase steps in the excitation patterns are equidistant. Thus, the sum of the excitation patterns I_φ over all five phases φ of each slice in each direction is a homogeneous pattern of intensity I_{sum}. As a consequence, the sum over all phases in the acquired raw images D_φ is equivalent to a wide-field image D of the specimen S imaged with the system's PSF h:

$$D(\vec{r}) = \sum_{\varphi=1}^{5} D_\varphi(\vec{r}) = \sum_{\varphi=1}^{5} \left(\left(S \cdot I_\varphi \right) \otimes \mathrm{h} \right)(\vec{r}) = \left(\left(S \cdot \sum_{\varphi=1}^{5} I_\varphi \right) \otimes \mathrm{h} \right)(\vec{r})$$

$$= \left(\left(S \cdot I_{sum} \right) \otimes \mathrm{h} \right)(\vec{r}) \propto \left(S \otimes h \right)(\vec{r}) \tag{1}$$

It should be pointed out, that summing up the phases removes all additional high resolution information from the data. In case of uneven phase steps, the wide-field image

could be obtained as the zero order out of the reconstruction procedure. Bleaching and laser fluctuations are eliminated by normalizing the intensity of each wide-field image.

2.2 Step B – create two independent wide-field images

To detect motion, a second wide-field image is needed for comparison. Images of different slices cannot be compared, since the defocus leads to notable changes in the image. The three different directions lead to three independent wide-field images. However, the excitation patterns of different orientations have quite significant differences for several reasons in an experimental setup: The excitation probability of each fluorophore often depends on the polarization of the incoming beam [13], especially for covalently bound labels. Due to the necessary azimuthal polarization of the illumination beams, the excitation rate of each fluorophore changes with the direction [8]. In addition to unprecise experimental control of the illumination intensity, the first order beams take individual ways through the cell, leading to different losses by absorption and scattering influencing the illumination brightness.

Although there is one wide-field image available after step A, there seems to be nothing to compare it with. Two independent wide-field images of the same focus slice have ideally to be created for each of the three illumination directions. This can be achieved by a detailed look into the theory of three-beam SIM, as given by Gustafsson et al. [3]:

All intensity orders of the illumination pattern have to be separated from each other to undo the introduced respective frequency shift. However, from the seven orders in 3D, only five can be separated (see Fig. 2). E.g. the two plus first orders, which have the same lateral shift in Fourier space but an opposing axial one, cannot be separated, because of their identical phase modulation. To allow a reconstruction nevertheless, the illumination pattern can be thought of as being attached to the detection PSF rather than to the specimen, which is caused by the illumination structure moving along Z while refocussing the specimen to acquire a stack. The opposing axial shift in Frequency space applies to the OTF $\tilde{H}$ of the detection. The reconstruction does therefore not need to perform any axial shifts in frequency space, but this effect is already accounted for by the acquisition process. Only the lateral shift (identical for each of these paired orders) remains for which the orders do not need to be separated. A consequence of the axially shifted OTF $\tilde{H}_{\pm 1}$ is that a higher axial sampling compared to widefield imaging is required to avoid aliasing. Since the illumination orders are diffraction limited by the objective too, the axial shift of the first order SIM-OTF $\tilde{H}_{\pm 1}$ cannot be bigger than the highest axial frequency support of the wide-field OTF $\tilde{H}_0$. Thus the sampling along z needs to be twice as fine as in standard wide-field microscopy.

Fortunately, the pseudo-wide-field image after step A does not contain any SIM information. Thus, the twice finer SIM sampling along z is redundant for this zero-order component. If every second focus slice was deleted, it would not lead to any loss of information, since the axial sampling is still under the Nyquist – limit. Therefore we can create two independent wide-field image stacks, by using the even z-slices on the one hand and the odd z-slices on the other (see Fig. 3) which can then be used for motion detection. However, requirement B is still not fulfilled, because both image stacks still have different planes of focus. With the help of the Fourier shift theorem, the foci of the even and odd slices are moved by half a slice up and down respectively, to meet halfway. Both so called *interlayer* (IL) images show the same focus plane and can be compared. The necessary multiplicative phase ramp in Fourier space $\tilde{K}_{up/down}\left(k_z\right)$ is scaled to the sampling frequency $k_{sampling}$:

$$\tilde{K}_{up/down}\left(k_z\right) = e^{\pm \frac{i\pi k_z}{2 \cdot k_{sampling}}} \qquad (2)$$

$$D_{even}^{(IL)}(\vec{r}) = \left(D_{even} \otimes K_{up}\right)(\vec{r}) \tag{3}$$

$$D_{odd}^{(IL)}(\vec{r}) = \left(D_{odd} \otimes K_{down}\right)(\vec{r}) \tag{4}$$
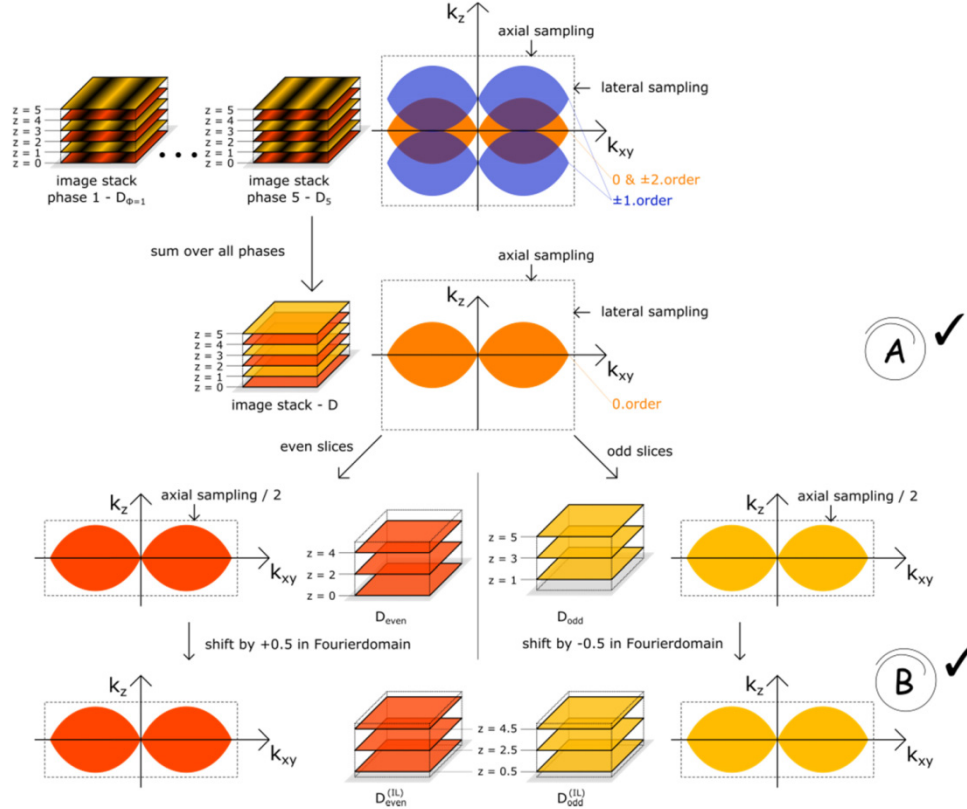

Fig. 3. Adding up all phases gives a standard wide-field image which is axially oversampled by a factor of two. Two independent wide-field image z-stacks are generated by separating even and odd slices. Their different focus position z is corrected in the Fourier domain. The frame-difference method can be applied to them.

2.3 Step C – Distinguish between noise and motion

The number of photons is always an issue in fluorescent imaging. So the frame difference $\Delta(\vec{r})$ of the corresponding interpolated wide-field images $D_{even}^{(IL)}(\vec{r})$ and $D_{odd}^{(IL)}(\vec{r})$ shows the motion overlaid with processed Poisson and the camera readout noise.

$$\Delta(\vec{r}) = D_{even}^{(IL)}(\vec{r}) - D_{odd}^{(IL)}(\vec{r}) \sim \left(S^{(IL)}(\vec{r}, t_0) - S^{(IL)}(\vec{r}, t_0 + \Delta t)\right) \otimes h \tag{5}$$

$$\triangleq \text{motion} + \text{Poisson and readout noise}$$

Nevertheless, summing up the images of all five grating phases in step A leads already to a five times higher photon number, which is high enough to treat the Poisson shot noise to be a symmetrical Gaussian distribution with a variance proportional to the brightness. It is possible to distinguish noise and motion if the standard deviation $\sigma\left[\Delta(\vec{r})\right]$ is known. Thus, $\sigma\left[\Delta(\vec{r})\right]$ is estimated out of the raw data $D_{\varphi}(\vec{r})$.

The variance $\sigma^2_{pois}\left[D_\varphi(\vec{r})\right]$ in a Poisson distribution is equal to its mean $\mu\left[D_\varphi(\vec{r})\right]$, which is estimated to be identical to the number of counted photoelectrons + 1. The additive 1 guarantees that at least one photoelectron is expected, although there was none detected in very dark areas. Thus, each measured pixel value $D_\varphi(\vec{r})$ has to be converted into the incoming number of photoelectrons by the known (from calibration) camera gain g. The variance of the Poisson noise in each raw image $\sigma^2_{pois}\left[D_\varphi(\vec{r})\right]$ is:

$$\sigma^2_{pois}\left[g\cdot D_\varphi(\vec{r})\right]=g^2\cdot\sigma^2_{pois}\left[D_\varphi(\vec{r})\right]$$

$$\sigma^2_{pois}\left[g\cdot D_\varphi(\vec{r})\right]=\mu\left[g\cdot D_\varphi(\vec{r})\right]\approx g\cdot D_\varphi(\vec{r})+1$$

$$\sigma^2_{pois}\left[D_\varphi(\vec{r})\right]\approx\frac{D_\varphi(\vec{r})}{g}+\frac{1}{g^2} \tag{6}$$

Finally, the total variance in each pixel of the raw data $\sigma^2\left[D_\varphi(\vec{r})\right]$ is the sum of the estimated photoelectron noise and the camera specific and constant readout noise σ^2_{dark}, which is obtained experimentally:

$$\sigma^2\left[D_\varphi(\vec{r})\right]=\sigma^2_{pois}\left[D_\varphi(\vec{r})\right]+\sigma^2_{dark} \tag{7}$$

The sum over all phases in step A applies directly as a sum of all variances
Eq. (1) →

$$\sigma^2\left[D(\vec{r})\right]=\sum_\varphi\sigma^2\left[D_\varphi(\vec{r})\right] \tag{8}$$

Separating the pseudo wide-field image $D(\vec{r})$ separates the variances into $\sigma^2\left[D_{even}(\vec{r})\right]$ and $\sigma^2\left[D_{odd}(\vec{r})\right]$, too. The final axial focus shift into the interlayer of the discrete sampling grid is done by a convolution with $K_{up/down}(z)$. To account for this operation, the variance has to be convolved with the square of the kernel $K^2_{up/down}(z)$. The convolution leads to correlated noise along z. However, computing the covariance matrix to capture the correlations is not required, because there is no further interaction among the pixels.
Eq. (3) →

$$\sigma^2\left[D^{(IL)}_{even}(\vec{r})\right]=\left(\sigma^2\left[D_{even}(\vec{r})\right]\otimes K^2_{up}(z)\right)(\vec{r}) \tag{9}$$

Eq. (4) →

$$\sigma^2\left[D^{(IL)}_{odd}(\vec{r})\right]=\left(\sigma^2\left[D_{odd}(\vec{r})\right]\otimes K^2_{odd}(z)\right)(\vec{r}) \tag{10}$$

Although calculating $\Delta(\vec{r})$ is a subtraction, the variances add.
Eq. (5) →

$$\sigma^2\left[\Delta(\vec{r})\right]=\sigma^2\left[D^{(IL)}_{even}(\vec{r})\right]+\sigma^2\left[D^{(IL)}_{odd}(\vec{r})\right] \tag{11}$$
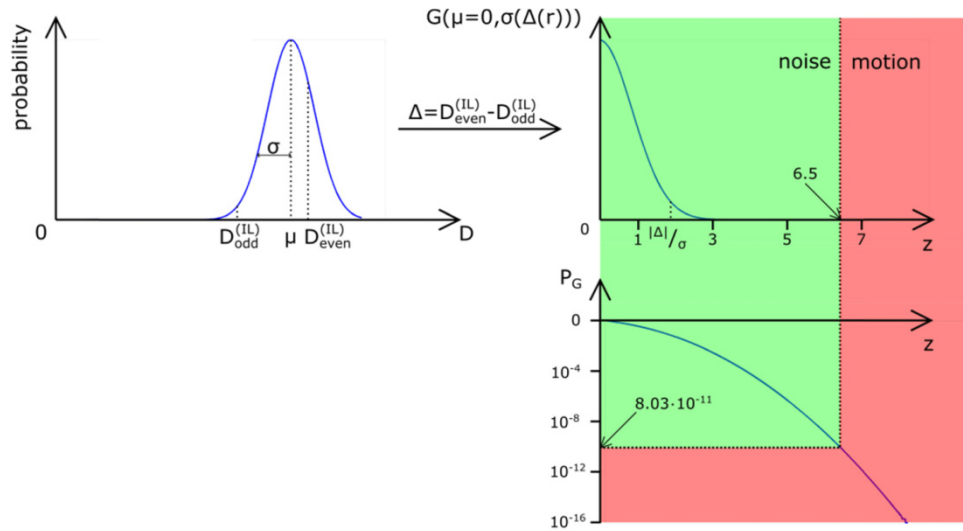
Fig. 4. Hypothesis test if the two measured values $D_{even}^{(IL)}\left(\vec{r}\right)$ and $D_{odd}^{(IL)}\left(\vec{r}\right)$ originate from the same, but unknown, Gaussian probability distribution (top left). Thus, the difference of both measurements Δ is scaled to its estimated standard deviation $\sigma\left[\Delta\left(\vec{r}\right)\right]$, which is the z-score z. (top right). If z is bigger than 6.5, the hypothesis is rejected and a movement must have occurred in the corresponding pixel (bottom right).

The decision whether the frame-difference $\Delta\left(\vec{r}\right)$ originates from noise only or not, is done for each pixel independently as illustrated in Fig. 4. The values $D_{even}^{(IL)}\left(\vec{r}\right)$ and $D_{odd}^{(IL)}\left(\vec{r}\right)$ are both single measurements out of an entire pixel dependent Gaussian probability distribution. If there is no motion i.e. both measurements originate from the same distribution, the same measurement was done twice. Thus their difference $\Delta\left(\vec{r}\right)$ is expected to be zero $\left(\mu\left[\Delta\left(\vec{r}\right)\right]=0\right)$. The *z-score* $z\left(\vec{r}\right)$ normalizes the measured deviation from the mean with respect to the estimated standard deviation $\sigma\left[\Delta\left(\vec{r}\right)\right]$:

$$z(\vec{r}):=\frac{\left|\Delta(\vec{r})-\mu\left[\Delta(\vec{r})\right]\right|}{\sigma\left[\Delta(\vec{r})\right]}=\frac{\left|\Delta(\vec{r})\right|}{\sigma\left[\Delta(\vec{r})\right]} \qquad (12)$$

The higher the z-score, the lower its probability to occur from random noise only. The Gaussian error function *erf* can be used to estimate the probability $P_G\left(\vec{r}\right)$ that a measured z-score $z\left(\vec{r}\right)$ – or and even higher one – occurred just by chance from the assumed hypothetical Gaussian distribution $\mathcal{G}\left(\mu=0,\sigma\left[\Delta\left(\vec{r}\right)\right]\right)$.

$$P_G\left(\vec{r}\right)=P\left(z\geq z(\vec{r})\mid \mathcal{G}\left(0,\sigma\left[\Delta(\vec{r})\right]\right)\right)$$

$$=1-P\left(z<z(\vec{r})\mid \mathcal{G}\left(0,\sigma\left[\Delta(\vec{r})\right]\right)\right)=1-\mathrm{erf}\left(\frac{z(\vec{r})}{\sqrt{2}}\right) \qquad (13)$$

We define that for $z\left(\vec{r}\right)>6.5$, which corresponds to a probability of $P_G\left(\vec{r}\right)<8.03\cdot10^{-11}$ (or one out of 12.5 billion), our hypothesis must be wrong. Hence $D_{even}^{(IL)}\left(\vec{r}\right)$ and $D_{odd}^{(IL)}\left(\vec{r}\right)$ cannot

originate from the same Gaussian distribution and the specimen must have moved. In comparison, one data set has around 25 million pixels (*[x, y, z] = [1000, 1000, ~25]*). The 3 orders of magnitude in between ensure that a negligible movement or experimental imperfections, such as aberrations or laser fluctuations, do not trigger a motion alert.

The algorithm can be further improved by considering the correlation between neighbouring pixels. The Gaussian noise in $D_{even}^{(IL)}(\vec{r})$ and $D_{odd}^{(IL)}(\vec{r})$, albeit being correlated along Z remains uncorrelated along X and Y and thus leads to a completely random sign in the difference image Δ. However, a moving fluorescent object changes the value of neighbouring pixels in the difference image in a correlated manner and leads to equal signs in an area of the size of the PSF (see Eq. (5)). By convolving the difference image with the PSF, noise will be reduced, because of its fluctuating sign while motion is maintained due to the consistent signs in the region. The variance has to be transformed by the square of the PSF again.

$$z_h(\vec{r}) = \frac{\left|(\Delta \otimes h)(\vec{r})\right|}{\sqrt{\left(\sigma^2 \otimes (h^2)\right)(\vec{r})}} \tag{14}$$

The hypothesis test is applied to all three illumination grating directions, which are finally combined by a maximum projection. In the next step, an erosion operation from mathematical morphology is performed, to remove salt and pepper noise. Afterwards, a dilation merges several small moving fluorescent objects to one bigger area of movement. The obtained motion indicator map is super-sampled to match the sampling of the high resolution SIM image. Finally, the motion map is subtracted from a dilated version of it, in order to get its border, which can be inserted as a red line in wide-field and SIM image.

3. Sample preparation and data acquisition

The algorithm was tested on the commercial SIM system Elyra S1 (Zeiss, Germany). We imaged living *stomata cells* in an ivy-leaf *(Epipremnum aureum)*. Stomata are in the lower epidermis layer at the bottom side of the leaf and have chloroplasts, which contain *thylakoid* clusters of autofluorescent chlorophyll. The cell layers inside the leaf (*mesophyll*) have much more chlorophyll and lead to a strong background signal. Thus, a scalpel is used to detach the lower epidermis from the mesophyll. Some chloroplasts are released from the cells, the scalpel is cutting through, and dissolve into the water the cell is embedded in. Thus we can compare a naturally fixed chloroplast in a stoma with a floating chloroplast in the embedding media. We ensured that our objects are chloroplasts by comparing them to the thylakoid studies of Rumak et al. [14].

The objective was a plan-apochromat oil-objective (63 × /1.4; Zeiss, Jena, Germany). The camera was an Andor iXon[EM] + (Andor, Belfast, Northern-Ireland). We measured gain (0.11e[-]/ADU) and readout noise (17.0 e[-] rms). The chlorophyll was excited by a 1.5 mW/642 nm laser and exposed for 400 ms in each raw image. Imaging with more laser power led to phototoxicity, which tore the cell layers apart. The autofluorescent signal passed a 655 nm longpass filter.

4. Results

In the presented data, there is a free chloroplast around 5 µm above the stoma in the lower epidermis. Thus, we had to acquire two z-stacks around the two different focus positions. One component is in focus, while the other is blurry background. First, we imaged a stack of 24 slices of the free chloroplast, afterwards 28 slices of the closed stoma in focus. Figure 5 shows the corresponding wide-field images as a sum over all phases and directions.
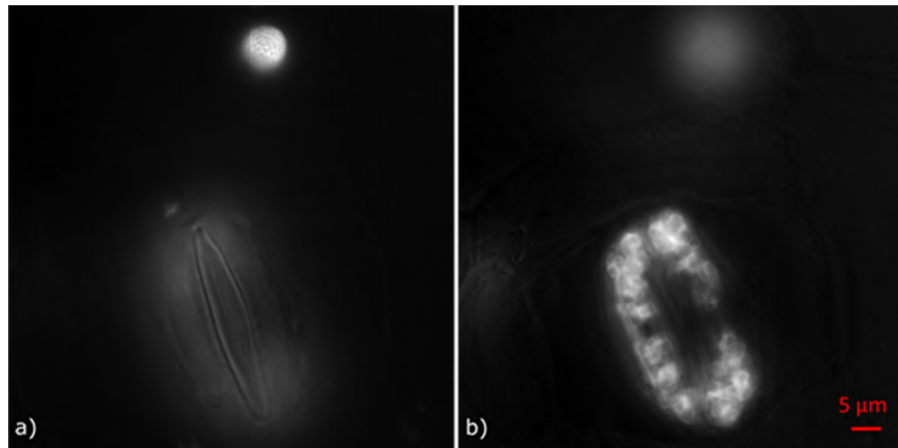
Fig. 5. Wide-field images out of a SIM z-stack focussed on a) a free chloroplast and b) a more stable stoma within the epidermis. Both layers are 5 μm apart.

Figure 6 shows a wide-field image of the free chloroplast at two adjacent z-planes. A motion – consisting of a shift and a rotation - of the entire chloroplast is visible and can be seen by comparing both slices; e.g.: one thylakoid leaves the red box from one z-plane to another. This is not the shape of a defocussed PSF and thus a clear motion. The shift of the thylakoids is up to 200nm (see b)). A rotation can be seen (rotation axis in blue).
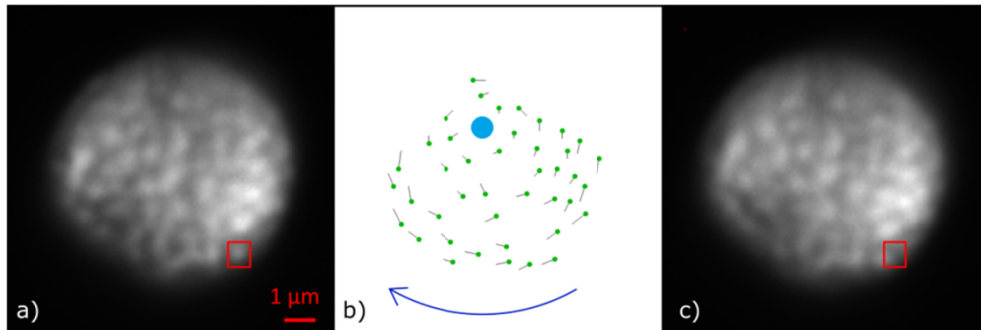
Fig. 6. Wide-field z-stack of a moving chloroplast out of SIM raw data ($\gamma = 1,8$). a) $z = z_0$ and c) $z = z_0 + 140$nm. The thylakoid moves out of the red box, which cannot be explained by the axial shape of the PSF. Thus, it has to be motion. b) The movement of each thylakoid is tracked by hand and displayed by the rods. The rotation axis is marked blue.

A slice by slice SIM reconstruction is affected less by motion. Each slice shows high resolution, as shown in Fig. 7(b). However, the 3-dimensional shape of the object is deformed, because the movement between the slices is maintained. It is rotating along z, as the raw images do, as it can be seen in Visualization 1 in the supplementary.
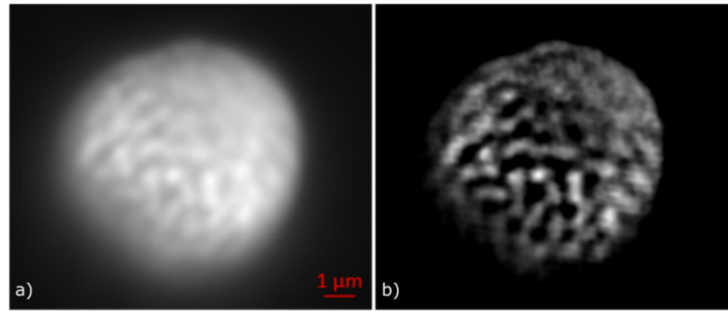
Fig. 7. a) wide-field and b) SIM image of a moving chloroplast. The SIM image provides higher resolution in a slice-per-slice reconstruction. However, the three-dimensional shape is distorted (Visualization 1).

A chloroplast is a comparatively big structure and moves slowly. Smaller structures, such as vesicles or even individual fluorophores, can move faster and lead to substantial artefacts in the SIM image (see Fig. 8). The occurring artefact is a grating and corresponds to the first excitation pattern direction. The second grating direction can be seen dimly as another artefact in the bottom right corner. This leads to the suspicion that the fluorophore left the shown region of interest (ROI) in this direction, while the second grating direction has been acquired. If the fluorophore had wiggled around without leaving the ROI, the three grating artefacts would have formed a honeycomb pattern.
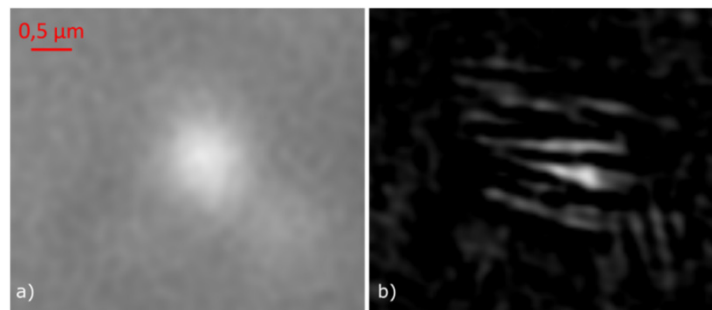

Fig. 8. a) wide-field and b) SIM image of a fast moving fluorophore. The reconstruction leads to a strong artefact.

Figure 9 shows all the image processing steps for the moving chloroplast at z = 1.61 μm. The wide-field image $D_{odd}^{(IL)}(\vec{r})$ is shown in a). The absolute difference image $\left|\Delta(\vec{r})\right|$ is shown in e). It shows clearly the moving chloroplast at the top and a few dim isolated particles. The stable stoma is almost invisible. The z-score $Z_h(\vec{r})$ in f) is calculated with the standard deviation $\sigma\left[\Delta(\vec{r})\right]$ in b). The filtered z-score $Z_h(\vec{r})$ in g) brings dim movements to light by reducing the noise. The threshold of $Z_h(\vec{r})$ forms the motion map in c). The chloroplast and dim particles are marked, while the stoma is not. The border of the motion map is shown in d) and put over the wide-field and the SIM-images in h). Visualization 2 and Visualization 3 in the supplementary show the image processing steps for all slices for the floating chloroplast and the stable stoma respectively. The SIM image is reconstructed by the standard routine of the used Elyra S1.
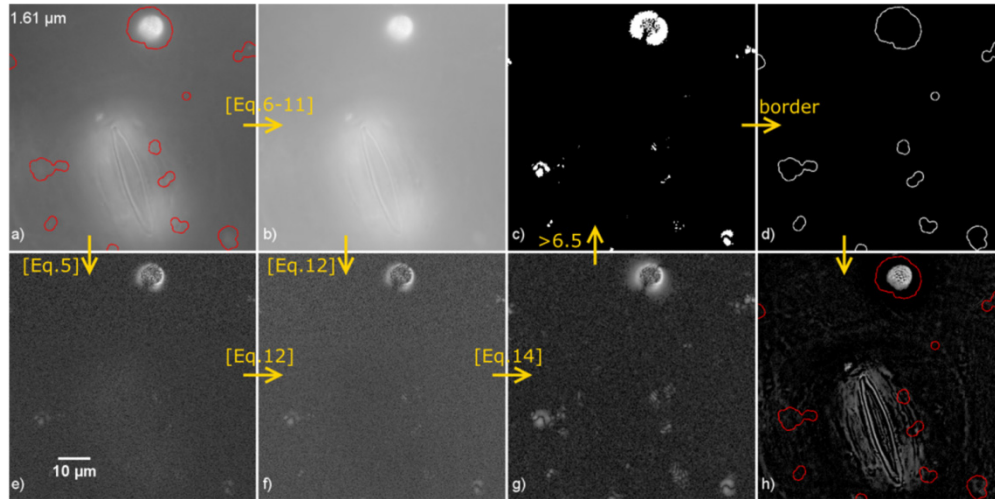
Fig. 9. Image Processing Steps marked by the yellow arrows ($\gamma = 0.35$): a) $D_{odd}^{(IL)}\left(\vec{r}\right)$ with motion in red; b) $\sigma\left[\Delta(\vec{r})\right]$; c) $z(\vec{r}) > 6.5$; d) border of $Z_h(\vec{r})$; e) $\left|\Delta(\vec{r})\right|$; f) $z(\vec{r})$; g) $Z_h(\vec{r})$; h) SIM-image with motion in red (Visualization 2 and Visualization 3).

Figure 10 shows the result of the motion detection algorithm applied to the acquired data sets. The red areas indicate motion-artefacts. The motion of the free chloroplast is completely detected in every focussed slice (left). A few small moving fluorescent particles are detected as well. The movement of the stoma is small (left and right). The movement of the low-contrast out-of-focus chloroplast (right) affects the image less, because only at its membrane, along the movement direction, the acquired signal of a pixel changes. This can be seen at the bottom of the chloroplast. Note that the scattering of emitted fluorescent light on the cell membranes makes them visible in the image, although they are not fluorescent on their own.

We tried several limits for the thresholding and found that the chosen value of 6.5 is good. Nevertheless, huge and bright moving object features, like the chloroplast, outshine their surroundings, so that a motion is detected in a slightly too big area. This is visible around the chloroplast in Fig. 10(a).
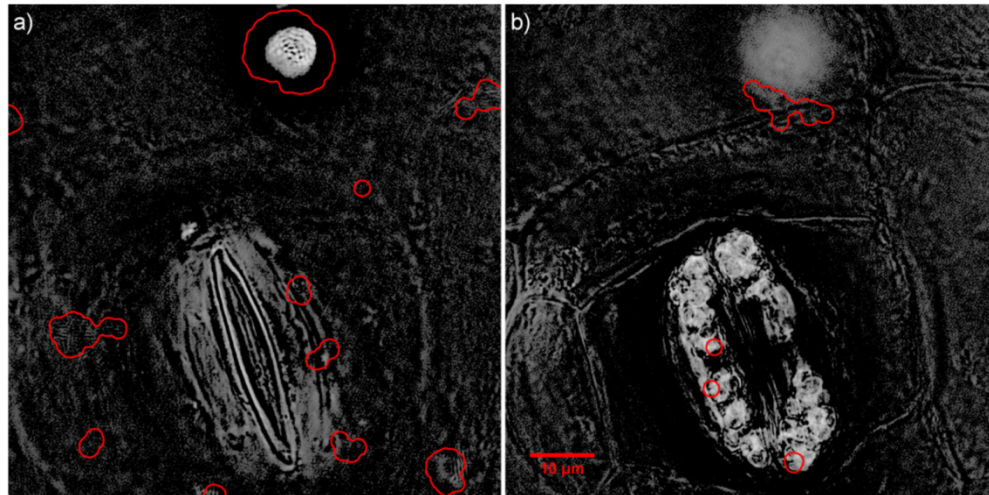
Fig. 10. SIM image of the stoma (left) and moving chloroplast (right). Movement artefacts are detected and encircled in red. ($\gamma = 0.25$ for a better visibility of low light artefacts.)

5. Conclusion

We developed a theory to detect and locate motion artefacts in SIM images and demonstrated our algorithm on a biological specimen for the first time. Motion artefacts have an unpredictable shape, so it is difficult to distinguish between artefacts and high resolution information of objects. Thus, it is necessary to spot the motion itself already in the raw data. We use the frame difference method (FDM) as a standard image processing routine. The necessary homogeneous excitation pattern is achieved by summing up all phases in each slice and direction in the raw images. Two independent wide-field images to spot a motion are obtained by taking advantage of the necessarily axially oversampled raw data. The FDM contains all the noise of the raw data. Thus, a detailed noise estimation and propagation is performed in order to distinguish between noise and motion. Areas with motion artefacts are encircled in the final SIM image.

The FDM can also be applied to two consecutive final SIM images. However, most acquisition configurations require the fast imaging of 30 stacks followed by a pause. The system should wait till starting the acquisition of the next image because bleaching and phototoxicity allow only a limited amount of images. Kner et al. acquired SIM images of living α-tubulin within 270ms, but just once per second [7]. The FDM of such consecutive images contains motion that happens mainly during the break and does not lead to SIM motion artefacts in the short time period of exposure. The same applies to consecutive multi-colour SIM, too.

The end user has several options to improve the image: increasing the laser power and reducing the exposure time, with the risk of phototoxicity and signal-to-noise problems respectively. If this is not sufficient, the cell has to be fixed or labelled with brighter fluorophores. It is also possible that a different microscopy technique is more suitable. With the help of our algorithm, the end-user gets the opportunity to know whether the SIM images are affected and damaged by motion or not.

6. Outlook

Our method requires a 3D data stack, which is not always available. Two-beam methods, like nonlinear SIM, do not have the axial resolution enhancement three-beam SIM has. Thus, there is only one sample plane acquired and our method is not executable. One solution is to use an additional phase step in the illumination pattern, in order to create two independent wide-field

images. Another possibility is to analyse the overlap area of the different SIM orders, which contain identical information in case of a perfect image acquisition. Any deviation may originate from a movement but not necessarily. This task is under current investigation.

The value of the threshold of the z-score to be 6.5 is set by empirical and simulated studies. We are going to apply our algorithm on a variety of live cell images, in order to find a more accurate way to determine the threshold.

Funding

Acknowledgments